

Systematic optimization of laser cooling of dysprosium

Florian Mühlbauer,^{1,*} Niels Petersen,^{1,2} Carina Baumgärtner,¹ Lena Maske,¹ and Patrick Windpassinger^{1,2}

¹*Institut für Physik, AG QUANTUM, Johannes Gutenberg-Universität Mainz, 55122 Mainz, Germany*

²*Graduate School Materials Science in Mainz, Staudingerweg 9, 55128 Mainz, Germany*

(Dated: April 6, 2018)

We report on an apparatus for cooling and trapping of neutral dysprosium. We characterize and optimize the performance of our Zeeman slower and 2D molasses cooling of the atomic beam by means of Doppler spectroscopy on a 136 kHz broad transition at 626 nm. Furthermore, we demonstrate the characterization and optimization procedure for the loading phase of a magneto-optical trap (MOT) by increasing the effective laser linewidth by sideband modulation. After optimization of the MOT compression phase, we cool and trap up to 10^9 atoms within 3 seconds in the MOT at temperatures of 9 μ K and phase space densities of $1.7 \cdot 10^{-5}$, which constitutes an ideal starting point for loading the atoms into an optical dipole trap and for subsequent forced evaporative cooling.

I. INTRODUCTION

Quantum gases composed of neutral atoms possessing large permanent magnetic ground-state dipole moments have proven to be a very successful platform for exploring dipolar physics in the quantum regime. These systems have led to the discovery of new quantum phases and quantum effects, for example the realization of the extended Bose-Hubbard model [1], the observation of the roton mode [2] and droplet formation [3–7]. Similar to these effects, which arise when the long-range, anisotropic magnetic dipole-dipole interaction (DDI) dominates the system, other exotic states of quantum matter are predicted for dipolar bosonic quantum gases in optical lattices, e.g. checkerboard or supersolid phases [8].

Due to these fascinating prospects, the interest in laser cooling of lanthanide atoms with large permanent magnetic dipole moments has grown rapidly within the last few years [9–21], as laser cooled atomic samples constitute the prerequisite for producing strongly magnetic degenerate quantum gases [22–26]. The generation of cold ensembles of lanthanide atoms in a magneto-optical trap (MOT) at temperatures of a few micro Kelvin has proven to be challenging [11, 22]. However, a very successful and convenient approach was demonstrated [16, 17], by making use of strong optical transitions in the blue spectral range for precooling of the atoms inside a Zeeman slower (ZS) before capturing them in a narrow-line MOT. Here, a slow atom beam is produced by using cooling transitions with a linewidth of several tens of Megahertz, whereas the MOT is operated on transitions with natural linewidths on the order of 100 kHz, resulting in Doppler temperatures below 5 μ K, which allows to directly transfer the atoms from the MOT into an optical dipole trap (ODT). Moreover, the interplay of radiation pressure cooling on narrow line transitions and gravitational forces lead to spin polarization of the atomic sample in the MOT [11, 16, 17, 19, 22], which allows for

describing the system with a two-level model.

Dysprosium possesses the highest permanent magnetic ground-state dipole moment in the periodic table alongside terbium, which makes it an ideal choice for performing quantum gas experiments with dipolar atoms. It belongs to the group of lanthanide elements whose characteristic open f-shell electron configuration $[\text{Xe}]4f^{10}6s^2$ with spin $S = 2$, orbital angular momentum $L = 6$ and total angular momentum $J = 8$ gives rise to its high magnetic moment of 10 Bohr magnetons ($\mu \sim 10 \mu_B$). Compared to alkali atoms, whose magnetic moments are on the order of only $\mu \sim 1 \mu_B$, the DDI in ultra-cold gases of dysprosium is about 100 times stronger. However, due to its low vapor pressure, temperatures exceeding 1000 °C are necessary to evaporate a sufficient amount of atoms from the dysprosium source material. This leads to high initial atomic velocities of several hundred meters per second, which have to be reduced considerably before trapping of the atoms can be achieved. For precooling and Zeeman slowing we employ a strong $J = 8 \rightarrow J' = 9$ transition at 421 nm [27–29] with a natural linewidth of $\Gamma_{421} = 2\pi \cdot 32$ MHz and a saturation intensity of $I_{421}^{\text{sat}} = 56$ mW/cm². This transition is also used for absorption imaging of the atomic cloud. Even though this is not a closed cycling transition, it is well suited due to its adequate branching ratio to the ground state [12, 13]. For the MOT, we use a $J = 8 \rightarrow J' = 9$ transition at 626 nm [29–31] with a natural linewidth of $\Gamma_{626} = 2\pi \cdot 136$ kHz, corresponding to a Doppler temperature of 3.2 μ K, and a saturation intensity of $I_{626}^{\text{sat}} = 72$ μ W/cm². It is a closed transition as decay into lower energy levels other than the ground state are forbidden by parity and angular momentum selection rules, thus making a repump laser for the MOT unnecessary.

This paper concentrates on the systematic optimization of different laser cooling parameters for dysprosium. The main part of the manuscript is organized in the following way: First we present our experimental setup (Sec. II), designed for cooling and trapping of dysprosium atoms and give detailed descriptions of the vacuum system (Sec. II A) and the laser system (Sec. II B). In sections III and

* muelhbau@uni-mainz.de

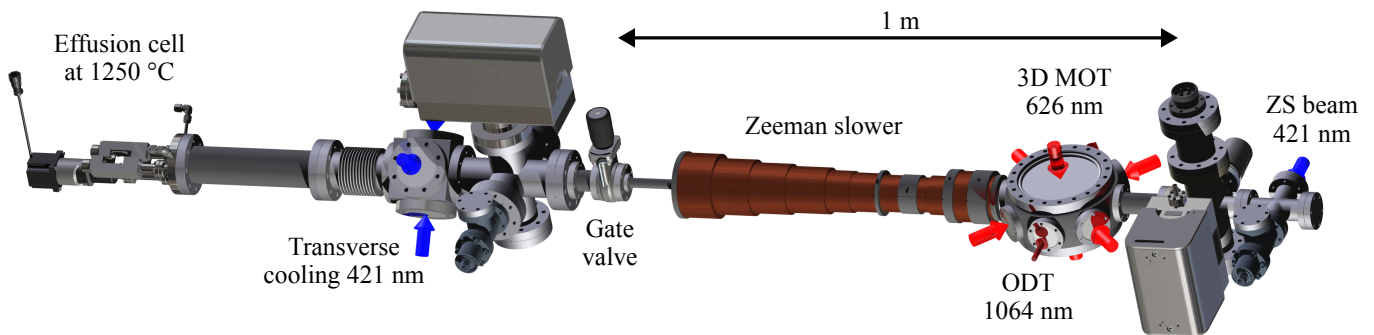


FIG. 1. CAD drawing of the vacuum system. In the oven chamber on the left hand side, Dy atoms are evaporated in an effusion cell and transversally cooled in a 2D molasses setup. After longitudinal deceleration inside the ZS the atoms are captured by the 3D MOT in the main chamber.

IV, we briefly summarize the experimental procedure and the methods employed for characterization and parameter optimization measurements, respectively. In section V we show the results obtained for the transverse 2D molasses cooling (Sec. V A), the Zeeman slower (Sec. V B) and for the MOT loading and compression phase (Sec. V C).

II. EXPERIMENTAL SETUP

Our experimental setup consists of an ultra-high vacuum chamber and a dedicated laser system to generate tunable, frequency stabilized laser radiation necessary for laser cooling of dysprosium. Experimental sequences are generated by a LabVIEW based computer program which controls a real-time sequence processor. In this section, we will present the vacuum system and the laser system in detail.

A. Vacuum system

To reduce the influence of undesired magnetic stray fields on the Dy atoms, the vacuum system is assembled exclusively from anti-ferromagnetic stainless steel components. Figure 1 shows a CAD drawing of the vacuum system. It consists of two parts: the oven chamber and the main chamber. Both parts are separated by a gate valve allowing us to vent them individually, e.g. for refilling of the oven (SVT Associates, Inc., SVTA-DF-10-450, 10cc), which is used for evaporating the dysprosium source material. It is attached to the main body of the oven chamber by means of a flexible bellow, thus allowing for adjustment of the atomic beam. A UHV 6-way cube equipped with four DN 63 viewports, provides excellent optical access for transverse cooling (TC) of the atomic beam. We have installed an aperture of 4 mm diameter in front of the TC cube to collimate the atomic beam and to protect the vacuum viewports from being coated with dysprosium. The oven chamber is pumped

by a 75 L/s ion pump, which maintains pressures below $8 \cdot 10^{-10}$ mbar during full oven operation.

Downstream of the gate valve, the ZS connects the oven chamber and the main chamber. The ZS coil assembly encloses a 750 mm long DN 16 vacuum pipe, which, due to its low conductance, acts as a differential pumping stage and is able to sustain pressure differences of at least two orders of magnitude. The main chamber consists of a spherical octagon (Kimball Physics, MCF800M-SphOct-G2C8-A), which provides all necessary optical access for the 3D MOT, absorption imaging and the optical dipole trap. It is attached to a supporting 6-way-cross, which incorporates a 45 L/s ion pump and a titanium sublimation pump, achieving vacuum pressures as low as $4 \cdot 10^{-11}$ mbar. We have placed a right-angle prism mirror with aluminum coating inside the vacuum chamber to deflect the 421 nm ZS laser beam towards the oven chamber, counter-propagating to the thermal atomic beam.

B. Laser system

The laser system is depicted schematically in Fig. 2. We produce the 421 nm laser radiation for TC, ZS and absorption imaging by second harmonic generation (SHG) in two homebuilt frequency doubling units, each one routinely delivering up to 220 mW of 421 nm light. These units consist of a temperature stabilized beta-barium borate (BBO) crystal placed inside a power enhancing bow-tie resonator, which is length stabilized onto the fundamental laser wavelength of 842 nm. We use a commercial 842 nm external cavity diode laser (ECDL), which is seeding two homebuilt tapered amplifiers (TA), providing up to 2 W of output power each. After the first TA, a small fraction of the 842 nm light is separated and frequency shifted by an acousto-optical modulator (AOM), set up in double pass configuration, before it is used to seed the second TA. In this way, we are able to generate red-detuned 421 nm light for the ZS and near-resonant 421 nm light for TC and absorption imaging by using only one fundamental laser. The fundamen-

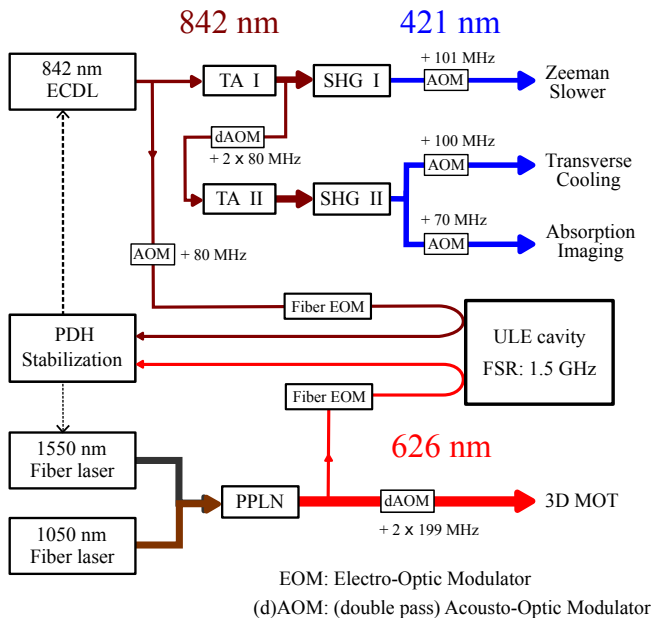


FIG. 2. Overview of the laser system. Starting with one 842 nm master ECDL and subsequent power amplification (TA) the 421 nm light is generated in two frequency doubling cavities (SHG), while the 626 nm light is generated by sum frequency mixing of the output light of two fiber lasers in a PPLN crystal. Frequencies are shifted via AOMs and EOMs with the fundamental lasers being stabilized via PDH offset-sideband locking to a ULE reference cavity.

tal 842 nm diode laser is frequency stabilized to an ultra-stable, ultra-low expansion (ULE) reference cavity with a free spectral range of 1.5 GHz by offset-sideband Pound-Drever-Hall (PDH) locking [32]. To this end, we modulate the diode laser current with a frequency of 20 MHz and use a fiber coupled electro-optical phase-modulator (EOM) to produce additional sidebands in the frequency range of 750 MHz to 1.5 GHz. In this way, we can produce PDH error signals for laser stabilization at any frequency between two adjacent ULE cavity resonances, thus allowing us to span the frequency difference between our ULE cavity and the resonance frequencies of all relevant dysprosium isotopes.

The orange 626 nm laser light for the 3D MOT is produced in a sum frequency mixing setup following the approach demonstrated by Wilson et al. [33]. The output light of two fiber-laser-amplifier systems (NKT Photonics, Koheras BoostiK E15 and Koheras BoostiK Y10 PM) with wavelengths of 1550 nm and 1050 nm is spatially overlapped and focused through a periodically poled lithium niobate (PPLN) crystal, where 626 nm laser radiation is produced by nonlinear frequency conversion. The crystal is placed inside a temperature stabilized oven to achieve quasi-phase matching and ensure optimal frequency conversion. For a maximum power of 5 W from both fiber lasers, this system generates up to 2.2 W of 626 nm output power. We also

use offset-sideband locking to enable easy switching between the different dysprosium isotopes. The local oscillator at 11 MHz for the PDH and the variable drive signal (750 MHz to 1.5 GHz) for the frequency offset are combined on a power splitter. The PDH error signals from the 626 nm light, which we couple to the ULE cavity, is fed back to the 1550 nm fiber laser, while the 1050 nm fiber laser remains free-running.

III. EXPERIMENTAL PROCEDURE

We operate the dual-filament high-temperature effusion cell at 1230 °C (1250 °C) in the main (tip) filament to produce a thermal atomic beam of dysprosium with a peak velocity of about 480 m/s. First, the atoms are laser cooled in transverse direction in order to reduce the beam divergence and hence increase the flux of atoms through the narrow ZS pipe into the main chamber. This is achieved in a 2D molasses cooling setup, where we employ the strong transition at 421 nm. We use two elliptical laser beams, set up in retro-reflex configuration, with $1/e^2$ diameters of 19 mm \times 5 mm to obtain a large overlap volume with the atomic beam. Laser cooling is typically achieved at a detuning of $-1 \Gamma_{421}$ and a laser power of 70 mW per transverse cooling beam, which corresponds to a mean intensity of $1.7 I_{421}^{\text{at}}$.

Next the atoms are longitudinally decelerated in the ZS to peak velocities of about 24 m/s before they enter the main chamber. We use a ZS in spin-flip configuration to limit the maximum absolute magnetic field strength to less than 250 G, which reduces the power consumption of the coil assembly to about 35 W. It consists of 11 individual coils, that are contacted in series to be supplied from the same current source with typically 9.5 A. The last coil at the end of the ZS is contacted opposite to the one before to reduce the residual magnetic field leaking out of the ZS into the proximity of the MOT. The theoretically calculated and measured magnetic field profiles of the commercially produced ZS (OSWALD Elektromotoren GmbH) are shown in Fig. 3a. To dissipate the heat produced from the coil assembly, we have implemented water-cooling between the vacuum chamber and the ZS pipe (40 mm inner diameter). With a water flow of about 10 L/min and a water temperature of 18 °C, we measure maximum temperatures of less than 25 °C during ZS operation on the surface of the coils. The laser cooling is achieved with typically 110 mW of circularly polarized 421 nm light. The cooling beam is focused towards the oven aperture and has a beam diameter of 14 mm ($1/e^2$) at the MOT position.

In the main chamber, slow atoms are captured by a six-beam 3D MOT, set up in retro-reflex configuration, which is operated on the closed, narrow line 626 nm transition. In order to reduce the influence of the 421 nm ZS beam passing through the MOT region, we have mounted the anti-Helmholtz coils 5 mm off-center with respect to the atomic beam axis (see Fig. 3c). Both coils have a

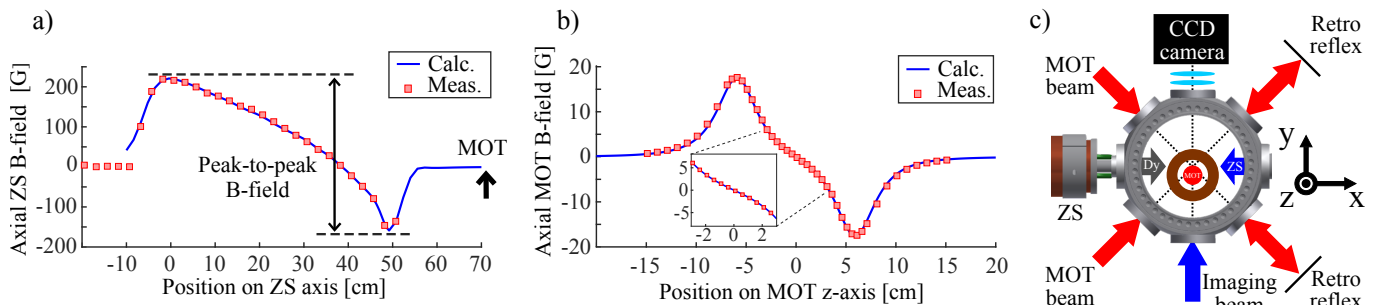


FIG. 3. (a) Axial magnetic field profile of the Zeeman slower (along the x-axis), operated at 9.5 A (simulation data from the manufacturer). The MOT position is marked by the arrow at 71 cm. (b) Axial magnetic field profile generated by the anti-Helmholtz coils (along the z-axis). The inset shows the magnetic field in the MOT region between ± 2 cm. (c) Schematic view of the MOT setup and the laser beam geometry for the ZS and the imaging system in the main chamber. The MOT coils (depicted as a copper ring) are displaced from the atomic beam axis by 5 mm to reduce the influence of the ZS beam on the atoms trapped in the MOT. Gravity is pointing along the negative z-axis.

mean diameter of 68 mm and are placed in a distance of 118 mm to each other. Figure 3b shows the measured and calculated axial magnetic field profile produced by the MOT coils. In the center, this setup provides a linear magnetic field gradient of about 40 mm spatial extent. The 626 nm laser beams are expanded to large diameters of 17 mm ($1/e^2$) to increase the MOT trapping volume. We increase the capture rate and the loading efficiency by artificial broadening of the 626 nm laser linewidth, which will be discussed in Sec. V C.

IV. METHODS

To characterize the velocity distribution of the atomic beam, we perform velocity sensitive fluorescence spectroscopy [34] on the 626 nm transition. Due to its narrow linewidth of 136 kHz, we can achieve higher resolution by utilizing this transition compared to the broader 421 nm transition. To this end, a collimated, circularly polarized 626 nm laser beam is sent through the main chamber to intersect with the atomic beam at the MOT position. While scanning the laser frequency across the atomic resonance, we collect the fluorescence photons with a photomultiplier mounted perpendicular to both the spectroscopy beam and the atomic beam. The relative angle between the probe beam and the atomic beam is henceforth denoted as α . Transverse velocity distributions can be measured if the probe beam is aligned to $\alpha = 90^\circ$, whereas longitudinal velocity distributions can be accessed for $\alpha \neq 90^\circ$. In the latter case, the Doppler shift of the atomic resonance frequency is given by $\omega_D = 2\pi f_D = kv \cos(\alpha)$. Here, k and v denote the modulus of the spectroscopy beam wavevector and the longitudinal velocity component of the atoms, respectively. For frequency to velocity conversion, we determine the zero-velocity reference frequency from a spectrum recorded at $\alpha = 90^\circ$. Due to the nonlinear conversion factor, velocities can be determined more precisely for smaller values of α , since uncertainties in its determi-

nation become less important for small angles. We use this technique to benchmark the performance of our ZS, as will be described in Sec. V B.

For characterization of the MOT, we use time-of-flight absorption imaging. Therefore, a large, collimated 421 nm laser beam with an $1/e^2$ diameter of 30 mm is aligned along the y-axis (perpendicular to the direction of gravity, see Fig. 3c) and covers enough space to image the atomic cloud for time-of-flights up to 30 ms. While imaging, we apply a weak magnetic field along the imaging axis to define a quantization and thus enhance the light-atom interaction cross-section due to favorable Clebsch-Gordan coefficients in the stretched Zeeman states. Typically, we use a laser power of 0.4 mW for imaging, corresponding to an intensity of $0.001 I_{421}^{\text{sat}}$ and detune the frequency by $1 \Gamma_{421}$ to avoid saturation effects during imaging.

V. RESULTS

In this section, we first summarize the characterization measurements of the TC, while the main focus will be the results of our optimization procedure for the ZS and the MOT. All measurements have been performed with the bosonic isotope ^{162}Dy , and have, for the ZS spectroscopy measurements, also been confirmed for the fermionic isotope ^{163}Dy and the most abundant bosonic isotope ^{164}Dy .

A. Transverse cooling

To characterize the transverse 2D molasses cooling in our setup, we perform fluorescence spectroscopy of the atomic beam, as described in Sec. IV. To this end, we align the probe beam to $\alpha = 90^\circ$ and record atom spectra for different TC beam intensities (example spectra see inset of Fig. 4). For each spectrum we determine the area below the peak, which we take as a measure for

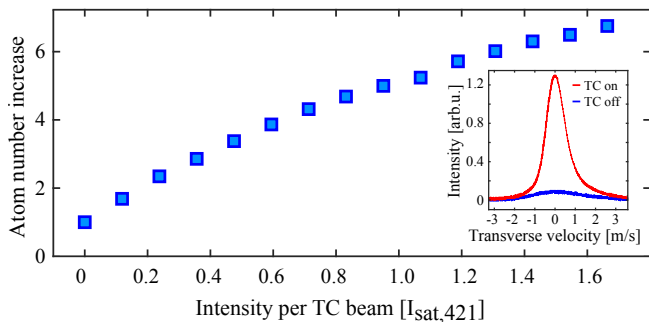


FIG. 4. Characterization of the TC setup. Atom number increase in the main chamber as a function of the TC beam intensity. Inset: Comparison of atom spectra for TC beams blocked (blue) and a TC beam intensity of $1.7 I_{421}^{\text{sat}}$ (red)

the atom number, and compare it to the area when the TC beams are blocked. Figure 4 shows a plot of relative atom numbers as a function of the TC beam intensity. We measure a continuous increase of atoms arriving in the main chamber with increasing TC beam intensity up to a mean intensity of $1.7 I_{421}^{\text{sat}}$, which corresponds to the maximum available laser power of 70 mW per TC beam in our experiment. To achieve optimal laser cooling, we use a TC beam detuning of $-1 \Gamma_{421}$, which has been determined independently with the same method. With the TC setup, we are able to increase the atomic flux in the main chamber by a factor of up to 6.5, which seems to be limited only by the available laser power, since we do not observe any significant saturation of atom numbers towards high TC beam intensities.

B. Zeeman Slower

We characterize the ZS performance by means of Doppler spectroscopy as described in Sec. IV and shown in Fig. 5. We adjust angles of $\alpha = 88.5^\circ$ between the atomic beam and the 626 nm probe beam in order to measure the full velocity distribution of the atomic beam (see Fig. 5a). One can clearly distinguish between the signal of thermal atoms peaked at about 480 m/s and the fraction of laser cooled atoms at ~ 24 m/s. We decrease α to 45° to be able to detect the fluorescence signal of the Zeeman-slowed atoms with better resolution (see Fig. 5b). Due to the large Doppler shift and Doppler broadening of the thermal atoms, their signal is well separated from the slow velocity part of the distribution, which is why we use the 45° spectroscopy setup to optimize the ZS parameters. To yield slow atom flux, the magnetic field and the laser detuning have to match the ZS resonance condition [35]. In order to determine the best operating range for our ZS, we measure slow atom spectra (as shown in Fig. 5b) for different combinations of ZS currents, i.e. different ZS peak-to-peak magnetic field strengths (as depicted in Fig. 3a), and ZS laser detunings. From these spectra we determine the peak velocity

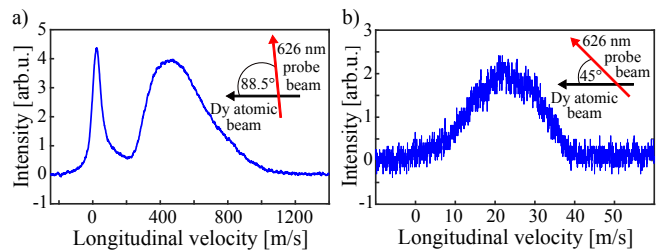


FIG. 5. Doppler spectroscopy of the atomic beam for two different scenarios. (a) For an angle of $\alpha = 88.5^\circ$ between the atomic beam and the probe beam, we measure the full velocity distribution of the atomic beam coming out of the ZS, which shows a clear signature of the slowed atoms at ~ 24 m/s. (b) We decrease the angle to $\alpha = 45^\circ$ in order to measure the slow velocity part of the distribution with higher resolution.

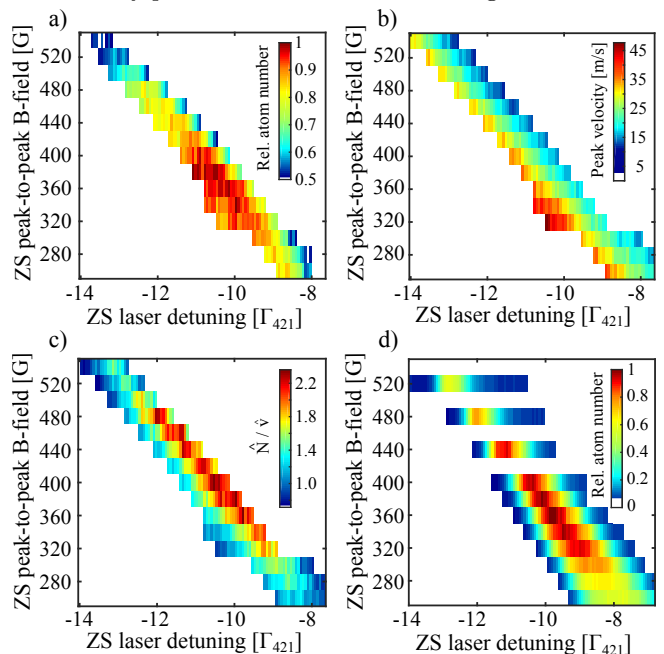


FIG. 6. ZS optimization measurements. (a) Map of slow atom numbers, normalized to the maximum value measured in the investigated parameter space. (b) Corresponding peak velocity map. For the determination of optimal ZS parameters with regard to MOT loading efficiency both the slow atom number and the peak velocity have to be taken into account. (c) Combination of atom number and velocity data to weight the amount of atoms with their velocity \hat{N}/\hat{v} . (d) Relative atom number map as a function of the ZS peak-to-peak magnetic field strength and ZS laser detuning determined by MOT fluorescence imaging.

and the area below the peak, which we take as a measure for the atom number. In this way, we investigate a parameter space between 260 G and 540 G of ZS peak-to-peak magnetic field strength and $-8 \Gamma_{421}$ to $-14 \Gamma_{421}$ of ZS laser detuning. We constrain our measurements to regions where the peak velocity of the distribution stays below 50 m/s, which is well beyond the capture range of the MOT. Figure 6a shows a map of relative atom num-

bers, which is normalized to the maximum atom number measured within the investigated parameter space. It shows a broad maximum for ZS peak-to-peak magnetic field strengths around 360 G. However, for the determination of optimal ZS parameters with regard to the MOT loading efficiency, both the amount of atoms and their velocity distribution have to be taken into account. Figure 6b shows a peak velocity map of the corresponding slow atom distributions. As can be seen, for given ZS peak-to-peak magnetic field strengths (horizontal trends), the peak velocities vary over a considerable range, which allows to further confine the ZS parameters to regions, where the peak velocity is low. To account for both criteria, we choose a representation (see Fig. 6c), in which we plot \hat{N}/\hat{v} , where \hat{N} denotes the relative atom number (as shown in Fig. 6a) and \hat{v} represents the corresponding peak velocities, normalized to the highest velocity measured. In order to obtain a preferably high number of atoms at low peak velocities we chose to operate the ZS at a peak-to-peak magnetic field strength of 380 G, which corresponds to a current of 9.5 A, and a laser detuning of $-10 \Gamma_{421}$.

To confirm whether the ZS parameter optimization, as described above, also accounts for optimal MOT loading, we have repeated the optimization procedure by MOT fluorescence imaging. Therefore, we load the MOT for different ZS parameters and detect the 626 nm fluorescence light with a CCD camera after 3 s of loading. Figure 6d shows a map of the MOT fluorescence signal, normalized to the maximum value measured. The trend agrees with the previous atomic beam spectroscopy measurements and also shows a broad range of ZS settings that lead to almost equally high atom numbers in the MOT. Our previously determined ZS parameters of a peak-to-peak magnetic field strength of 380 G and $-10 \Gamma_{421}$ fit very well with the MOT fluorescence optimization measurements, where we measure maximum atom numbers for ZS peak-to-peak magnetic field strengths in the range between 340 G and 400 G and ZS laser detunings between -9 and $-11 \Gamma_{421}$. We thus find that in our setup we are able to optimize the ZS parameters individually either by fluorescence spectroscopy of the atomic beam or by fluorescence imaging and atom number optimization of the MOT.

C. Magneto-optical trap

1. MOT loading:

During the loading phase of the MOT, we artificially broaden the 626 nm laser linewidth via sideband modulation inside an AOM [36, 37]. To this end, we modulate the AOM drive signal sinusoidally with a frequency of 136 kHz. Depending upon the modulation amplitude, this generates a comb-like frequency spectrum around the central laser frequency of variable width, which we characterize in a beat-note detection scheme with an unmod-

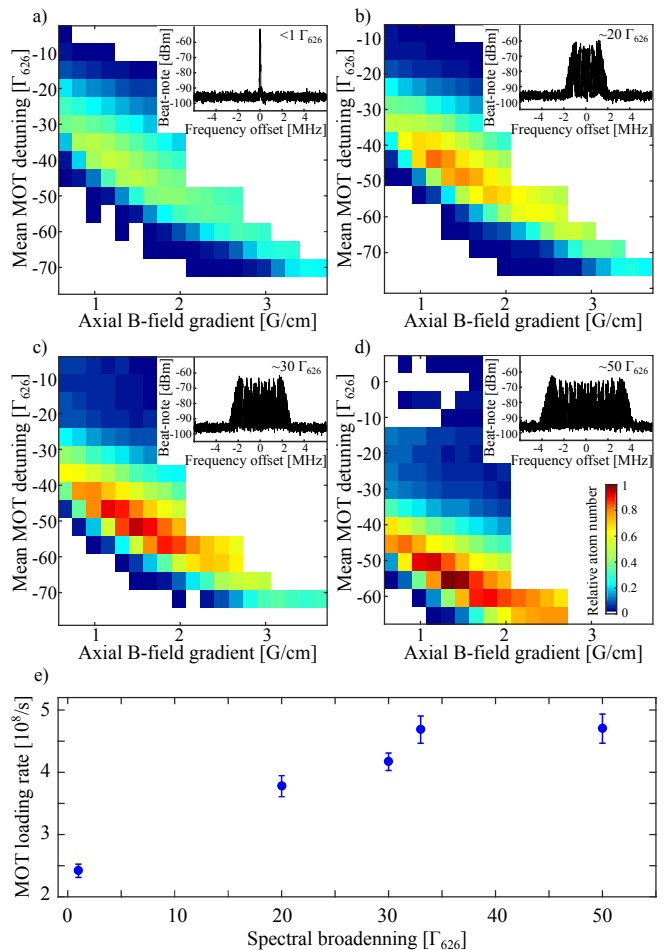


FIG. 7. MOT loading phase optimization. The plots show relative atom number maps for four different settings of spectral broadening as a function of the mean MOT laser detuning and the axial magnetic field gradient, measured after 3 s of loading. The insets show beat-note measurements of the MOT laser for the respective setting of spectral broadening. All four plots share the same color code for the atom numbers, which have been normalized to the overall maximum atom number. (a) No broadening. (b) $20 \Gamma_{626}$. (c) $30 \Gamma_{626}$. (d) $50 \Gamma_{626}$. (e) Comparison of MOT loading rates for different effective laser linewidths, measured with optimized parameters.

ulated laser beam (see Fig. 7 insets). In this way, we are able to increase the effective laser linewidth from a few tens of Kilohertz up to 6.8 MHz. We investigate its influence on the loading behavior of our MOT by determining the trapped atom number after a constant loading time of 3 seconds for different effective laser linewidths. For each setting we investigate a parameter space between axial magnetic field gradients of 0.7 G/cm to 3.5 G/cm and mean laser detunings of $-10 \Gamma_{626}$ to $-75 \Gamma_{626}$. Here, the mean laser detuning denotes the frequency difference between the center frequency of the spectrally broadened laser light and the atomic resonance, which we can adjust via the fiber EOM while keeping the spectral broadening at a constant level. We use 120 mW per MOT beam,

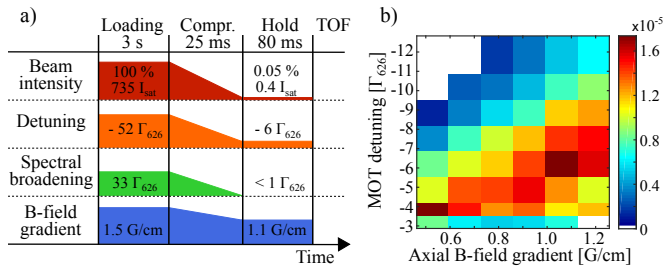


FIG. 8. MOT compression phase optimization. (a) Schematic drawing of the experimental sequence. After 3 s of loading, we compress the MOT within 25 ms to reduce the temperature and to increase the density. The atoms are held for 80 ms before we start the TOF sequence. (b) Phase space density map as function of the final axial magnetic field gradient and the final MOT detuning at the end of the compression phase.

which corresponds to a mean intensity of $735 I_{626}^{\text{sat}}$, in order to saturate all additional frequency components. Figure 7 shows atom number plots, normalized to the overall maximum atom number, for four different effective laser linewidths (no broadening, $20 \Gamma_{626}$, $30 \Gamma_{626}$ and $50 \Gamma_{626}$, see Fig. 7a-d). As the linewidth is increased, more atoms can be captured, when the mean laser detuning is increased as well to keep all additional frequency components red detuned from the atomic resonance. By measuring loading curves for MOT parameters that lead to maximum atom numbers for different effective laser linewidths, we observe that the loading rates begin to saturate at an effective laser linewidth of about $33 \Gamma_{626}$ (see Fig. 7e). We use this setting for the loading phase of the MOT with a mean detuning of $-52 \Gamma_{626}$ and a magnetic field gradient of 1.5 G/cm.

2. MOT compression:

To increase the density and to reduce the temperature of the atomic cloud, we subsequently compress the MOT by simultaneously ramping down the laser beam intensity, the mean laser detuning, the magnetic field gradient and the MOT light broadening in a linear way. Afterwards, we hold the atoms in the trap for 80 ms to let them equilibrate before we take time-of-flight absorption images. By varying the compression time between 25 ms and 400 ms, we observe that twice as many atoms are lost for 400 ms compared to 25 ms, while the final temperature and the density do not change significantly. For this reason, we use 25 ms in the compression phase. We also investigate the influence of the laser detuning and the magnetic field gradient after the compression ramp on

the atom number, the temperature and the phase space density. As a consequence, we load the MOT for 3 s and vary the final laser detuning and the final magnetic field gradient at the end of the compression ramp in a parameter space between $-3 \Gamma_{626}$ and $-12 \Gamma_{626}$ and 0.5 G/cm to 1.2 G/cm. We observe that within the investigated parameter space the atom number predominantly exceeds $9 \cdot 10^8$ and the temperatures are lower than 12 μK , without major differences. However, when considering the phase space density [38], one can clearly see a distinct maximum at $-6 \Gamma_{626}$ and 1.1 G/cm (see Fig. 8b).

Figure 8a shows a schematic of our optimized experimental sequence for MOT loading and compression. After a MOT loading time of 3 seconds we simultaneously reduce the mean laser beam intensity from $735 I_{626}^{\text{sat}}$ to $0.4 I_{626}^{\text{sat}}$, the mean laser detuning from $-52 \Gamma_{626}$ to $-6 \Gamma_{626}$, the spectral broadening width from $33 \Gamma_{626}$ to the laser linewidth and the magnetic field gradient from 1.5 G/cm to 1.1 G/cm. With this optimized sequence, we are able to trap 10^9 dysprosium atoms at a temperature of 9 μK and a phase space density of $1.7 \cdot 10^{-5}$, which constitutes a good starting point for transferring the atoms into an optical dipole trap and for subsequent forced evaporative cooling.

VI. CONCLUSION

We have presented our apparatus for cooling and trapping of neutral dysprosium and we have shown extensive parameter optimization measurements for the Zeeman slower and the magneto-optical trap. We have discussed, how we can optimize the ZS performance by two independent methods, which we find in good agreement with one another. For our ^{162}Dy MOT, we have investigated the influence of artificial laser linewidth broadening on the atom number and have determined optimal parameters for the MOT loading phase. Finally, we have studied the achievable atom numbers, temperatures and phase space densities of the compressed MOT and with optimized parameters we are able to trap 10^9 dysprosium atoms at a temperature of 9 μK and a phase space density of $1.7 \cdot 10^{-5}$. We believe that our results can be helpful for other experiments with cold lanthanide atoms, especially during the building phase.

ACKNOWLEDGMENTS

We gratefully acknowledge financial support by the JGU-Startup funding, DFG-Grossgerät INST 247/818-1 FUGG and the Graduate School of Excellence MAINZ.

[1] S. Baier, M.J. Mark, D. Petter, K. Aikawa, L. Chomaz, Z. Cai, M. Baranov, P. Zoller, F. Ferlaino, Science

- [2] L. Chomaz, R.M.W. van Bijnen, D. Petter, G. Faraoni, S. Baier, J.H. Becher, M.J. Mark, F. Waechtler, L. Santos, F. Ferlaino, arXiv:1705.06914 [cond-mat.quant-gas] (2017)
- [3] I. Ferrier-Barbut, H. Kadau, M. Schmitt, M. Wenzel, T. Pfau, Physical Review Letters **116**(21), 215301 (2016)
- [4] I. Ferrier-Barbut, M. Schmitt, M. Wenzel, H. Kadau, T. Pfau, Journal of Physics B: Atomic, Molecular and Optical Physics **49**(21), 214004 (2016)
- [5] H. Kadau, M. Schmitt, M. Wenzel, C. Wink, T. Maier, I. Ferrier-Barbut, T. Pfau, Nature **530**(7589), 194 (2016)
- [6] M. Schmitt, M. Wenzel, F. Böttcher, I. Ferrier-Barbut, T. Pfau, Nature **539**(7628), 259 (2016)
- [7] L. Chomaz, S. Baier, D. Petter, M. Mark, F. Wächtler, L. Santos, F. Ferlaino, Physical Review X **6**(4), 041039 (2016)
- [8] T. Lahaye, C. Menotti, L. Santos, M. Lewenstein, T. Pfau, Reports on Progress in Physics **72**(12), 126401 (2009)
- [9] J.J. McClelland, J.L. Hanssen, Physical review letters **96**(14), 143005 (2006)
- [10] A.J. Berglund, S.A. Lee, J.J. McClelland, Physical Review A **76**(5), 053418 (2007)
- [11] A.J. Berglund, J.L. Hanssen, J.J. McClelland, Physical Review Letters **100**(11), 113002 (2008)
- [12] N. Leefer, A. Cingöz, B. Gerber-Siff, A. Sharma, J. Torgerson, D. Budker, Physical Review A **81**(4), 043427 (2010)
- [13] S.H. Youn, M. Lu, B.L. Lev, Physical Review A **82**(4), 043403 (2010)
- [14] S.H. Youn, M. Lu, U. Ray, B.L. Lev, Physical Review A **82**(4), 043425 (2010)
- [15] D. Sukachev, A. Sokolov, K. Chebakov, A. Akimov, S. Kanorsky, N. Kolachevsky, V. Sorokin, Physical Review A **82**(1), 011405 (2010)
- [16] A. Frisch, K. Aikawa, M. Mark, A. Rietzler, J. Schindler, E. Zupanič, R. Grimm, F. Ferlaino, Physical Review A **85**(5), 051401 (2012)
- [17] T. Maier, H. Kadau, M. Schmitt, A. Griesmaier, T. Pfau, Optics Letters **39**(11), 3138 (2014)
- [18] J. Miao, J. Hostetter, G. Stratis, M. Saffman, Physical Review A **89**(4), 041401 (2014)
- [19] D. Dreon, L.A. Sidorenkov, C. Bouazza, W. Maineult, J. Dalibard, S. Nascimbene, Journal of Physics B: Atomic, Molecular and Optical Physics (2017)
- [20] E. Lucioni, G. Masella, A. Fregosi, C. Gabbanini, S. Gozzini, A. Fioretti, L. Del Bino, J. Catani, G. Modugno, M. Inguscio, The European Physical Journal Special Topics **226**(12), 2775 (2017)
- [21] P. Ilzhöfer, G. Durastante, A. Patscheider, A. Trautmann, M.J. Mark, F. Ferlaino, arXiv:1711.07378 [cond-mat.quant-gas] (2017)
- [22] M. Lu, N.Q. Burdick, S.H. Youn, B.L. Lev, Physical Review Letters **107**(19), 190401 (2011)
- [23] M. Lu, N.Q. Burdick, B.L. Lev, Physical Review Letters **108**(21), 215301 (2012)
- [24] K. Aikawa, A. Frisch, M. Mark, S. Baier, A. Rietzler, R. Grimm, F. Ferlaino, Physical Review Letters **108**(21), 210401 (2012)
- [25] K. Aikawa, A. Frisch, M. Mark, S. Baier, R. Grimm, F. Ferlaino, Physical Review Letters **112**(1), 010404 (2014)
- [26] Y. Tang, N.Q. Burdick, K. Baumann, B.L. Lev, New Journal of Physics **17**(4), 045006 (2015)
- [27] N. Leefer, A. Cingöz, D. Budker, Optics letters **34**(17), 2548 (2009)
- [28] M. Lu, S.H. Youn, B.L. Lev, Physical Review A **83**(1), 012510 (2011)
- [29] W.C. Martin, R. Zalubas, L. Hagan, NSRDS-NBS, Washington: National Bureau of Standards, US Department of Commerce,— c1978 (1978)
- [30] W. Hogervorst, G. Zaal, J. Bouma, J. Blok, Physics Letters A **65**(3), 220 (1978)
- [31] M. Gustavsson, H. Lundberg, L. Nilsson, S. Svanberg, JOSA **69**(7), 984 (1979)
- [32] J.I. Thorpe, K. Numata, J. Livas, Optics Express **16**(20), 15980 (2008)
- [33] A.C. Wilson, C. Ospelkaus, A. VanDevender, J.A. Mlynek, K.R. Brown, D. Leibfried, D.J. Wineland, Applied Physics B: Lasers and Optics **105**(4), 741 (2011)
- [34] J.V. Prodan, W.D. Phillips, H. Metcalf, Physical Review Letters **49**(16), 1149 (1982)
- [35] W.D. Phillips, H. Metcalf, Physical Review Letters **48**(9), 596 (1982)
- [36] T. Kuwamoto, K. Honda, Y. Takahashi, T. Yabuzaki, Physical Review A **60**(2), R745 (1999)
- [37] S. Dörscher, A. Thobe, B. Hundt, A. Kochanke, R. Le Targat, P. Windpassinger, C. Becker, K. Sengstock, Review of Scientific Instruments **84**(4), 043109 (2013)
- [38] C. Townsend, N. Edwards, C. Cooper, K. Zetie, C. Foot, A. Steane, P. Szriftgiser, H. Perrin, J. Dalibard, Physical Review A **52**(2), 1423 (1995)